PROCEEDINGS OF SPIE

SPIEDigitalLibrary.org/conference-proceedings-of-spie

Probing infrared detectors through energy-absorption interferometry

Dan Moinard
Stafford Withington
Christopher N. Thomas

SPIE.

Probing infrared detectors through energy-absorption interferometry

Dan Moinard[a], Stafford Withington[a], and Christopher N. Thomas[a]

[a]Cavendish Laboratory, Univ. of Cambridge, J. J. Thomson Avenue, Cambridge CB3 0HE, UK

ABSTRACT

We describe an interferometric technique capable of fully characterizing the optical response of few-mode and multi-mode detectors using only power measurements, and its implementation at 1550 nm wavelength. Energy-Absorption Interferometry (EAI) is an experimental procedure where the system under test is excited with two coherent, phase-locked sources. As the relative phase between the sources is varied, a fringe is observed in the detector output. Iterating over source positions, the fringes' complex visibilities allow the two-point detector response function to be retrieved: this correlation function corresponds to the state of coherence to which the detector is maximally sensitive. This detector response function can then be decomposed into a set of natural modes, in which the detector is incoherently sensitive to power. EAI therefore allows the reconstruction of the individual degrees of freedom through which the detector can absorb energy, including their relative sensitivities and full spatial forms. Coupling mechanisms into absorbing structures and their underlying solid-state phenomena can thus be studied, with direct applications in improving current infrared detector technology. EAI has previously been demonstrated for millimeter wavelength. Here, we outline the theoretical basis of EAI, and present a room-temperature 1550 nm wavelength infrared experiment we have constructed. Finally, we discuss how this experimental system will allow us to study optical coupling into fiber-based systems and near-infrared detectors.

Keywords: Energy-absorption interferometry, detectors, modes, optical measurements, optical fibers, near-infrared

1. INTRODUCTION

Understanding the optical response of absorbing structures is critical to the successful realization of any imaging instrument, including the maximization of performance characteristics such as throughput and detection efficiency. Such properties are critically dependent not only on the absorber's power reception pattern, but also on the full spatial forms and relative responsitivities of the absorber's natural modes, defined as the set of individually fully-coherent patterns for which the optical response is independent. This can be illustrated in the context of optical detectors, for instance. In the case of a single-mode detector and monochromatic source, the detector output is directly proportional to the coupling between the beam patterns of the detector and the source field; in the case of a highly-multimode detector and wideband source, radiometric techniques can be used.[1] Here, we also consider the intermediate regime where the detector is few-moded.

In this paper, we propose the use of a technique called Energy-Absorption Interferometry (EAI),[2,3] to fully characterize the optical behavior of near-infrared detectors. Saklatvala and Withington[4] have previously shown that a detector's optical behavior can be fully parametrized using a two-point response dyadic. The output of any power detector can be written as the contraction of this detector response function (DRF), corresponding to the spatio-temporal state of coherence of the detector response, with a second two-point dyadic representing to the state of coherence of the incident radiation.[5] Both states of coherence are completely general, such that the behavior of single-mode and massively multi-mode detectors can be obtained as limiting cases. The DRF may be interpreted equivalently in a modal picture, by decomposing it in terms of the detector's natural modes. The DRF is thus expressed as the incoherent superposition of these fully coherent response patterns, with the

Further author information: (Send correspondence to D.M.)
D.M.: E-mail: dm674@cam.ac.uk, Telephone: +44 (0)1223 766468
S.W.: E-mail: stafford@mrao.cam.ac.uk, Telephone: +44 (0)1223 337393

Infrared Sensors, Devices, and Applications VII, edited by Paul D. LeVan, Ashok K. Sood, Priyalal Wijewarnasuriya, Arvind I. D'Souza, Proc. of SPIE Vol. 10404, 104040J
 · doi: 10.1117/12.2271622

number of such terms corresponding to the number of intrinsic detector modes. EAI is used to measure the DRF experimentally, and recovers the state of coherence of the incident field to which the system is maximally sensitive.

To perform EAI, two coherent sources are used to illuminate the detector under test. As their relative phase is varied, the detector output forms a fringe, the complex amplitude of which is an element of the DRF in the basis of source locations. Iterating over source locations and polarizations, a matrix of complex fringe amplitudes can be constructed, which contains the necessary information to fully recover the detector response function. Through diagonalization, the spatial form and polarization patterns of the modes of the field in which the detector incoherently absorbs power, as well as their respective responsivities, are reconstructed.[6] The data analysis can be formulated using vectors and their duals, such that the convergence towards the system's unknown number of modes as measurement data is accumulated can also be studied.

In practice, in order to achieve EAI, various key components must be brought together, as was demonstrated in a previous proof-of-concept experiment at radio wavelengths.[3] The required capabilities include generating highly-coherent radiation, manipulating the relative phase of two beams, placing two probes accurately and measuring the absorbed radiation accurately. The design of an EAI experimental system suitable for the study of detectors and optical fibers operating in the near-infrared wavelength range has several key differences. We illustrate these here by detailing specific choices made for our own experimental system, and showing it will allow us to find the electromagnetic modes through which power is coupled into simple near-infrared detectors.

The first section of this paper will review the essential parts of the theory, including important results such as a coupled-mode theory for the output of a power detector, and critical concepts such as the DRF and how it can be retrieved and reconstructed in multiple suitable bases. The second section will summarize the design of an EAI experiment to study near-infrared detectors, as well as optical fibers operating at those wavelengths. As part of this, we will discuss the required capabilities of the experiment, propose a set of components that fit these requirements, and describe the additional steps we have taken to optimize the performance of our experimental system.

2. THEORY

2.1 Coupled-mode theory

Starting from linear systems theory and the fundamental assumption that the output of an ideal power detector must be quadratic in the incident field, Withington and Saklatvala[1,5] have shown that the power output of an ideal power detector is the total spatial contraction of two dyadic functions, $\overline{\overline{\mathbf{D}}}(\boldsymbol{r}_1, \boldsymbol{r}_2)$ and $\overline{\overline{\mathbf{E}}}(\boldsymbol{r}_1, \boldsymbol{r}_2)$ corresponding to the states of coherence of the detector response and incident radiation, respectively. The detector behavior is fully characterized by this two-point DRF $\overline{\overline{\mathbf{D}}}(\boldsymbol{r}_1, \boldsymbol{r}_2)$. Assuming only that the detector bandwidth and observation time are finite, and that the incident field is quasi-monochromatic, we obtain

$$\langle P \rangle = \iint_{\mathcal{S}^2} \overline{\overline{\mathbf{D}}}^{\dagger}(\boldsymbol{r}_1, \boldsymbol{r}_2) \cdot\cdot \overline{\overline{\mathbf{E}}}(\boldsymbol{r}_1, \boldsymbol{r}_2) d^2\boldsymbol{r}_1 d^2\boldsymbol{r}_2, \tag{1}$$

where $\mathcal{S}$ is the chosen integration surface, and $\overline{\overline{\mathbf{E}}}(\boldsymbol{r}_1, \boldsymbol{r}_2) = \langle \boldsymbol{E}(\boldsymbol{r}_1) \boldsymbol{E}(\boldsymbol{r}_2) \rangle$ is the field correlation dyadic, with $\boldsymbol{E}(\boldsymbol{r})$ denoting the incident analytical field, which could be partially coherent. Equation (1) is an inner product in a mixed tensor space: the measured power is described as the orthogonal projection of the incident radiation tensor field $\overline{\overline{\mathbf{E}}}(\boldsymbol{r}_1, \boldsymbol{r}_2)$ onto the detector response tensor field $\overline{\overline{\mathbf{D}}}(\boldsymbol{r}_1, \boldsymbol{r}_2)$. The DRF therefore corresponds to the dyadic field to which the detector is maximally sensitive. The DRF includes any polarization-dependent behavior by the detector, although we choose to suppress this here by assuming that a single polarization throughout for simplicity. We also remark that the integration surface $\mathcal{S}$ appearing in Equation (1) can be any surface where the form of the probe fields is known. For instance, it could be chosen to be the detector plane, some plane from which the external field $\boldsymbol{E}(\boldsymbol{r})$ is emitted, or any intermediate surface, simply by projecting both dyadics fields onto the chosen surface.

$\overline{\overline{\mathbf{E}}}(\boldsymbol{r}_1, \boldsymbol{r}_2)$ is Hermitian by definition. Withington and Saklatvala have shown that $\overline{\overline{\mathbf{D}}}(\boldsymbol{r}_1, \boldsymbol{r}_2)$ must also be Hermitian for the detector to behave physically,[1] such that both dyadic fields have a Hilbert-Schmidt decomposition:

$$\begin{aligned}\overline{\overline{\mathbf{E}}}(\boldsymbol{r}_1, \boldsymbol{r}_2) &= \sum_n \beta_n \boldsymbol{U}_n(\boldsymbol{r}_1)\boldsymbol{U}_n^*(\boldsymbol{r}_2) \\ \overline{\overline{\mathbf{D}}}(\boldsymbol{r}_1, \boldsymbol{r}_2) &= \sum_m \alpha_n \boldsymbol{R}_m(\boldsymbol{r}_1)\boldsymbol{R}_m^*(\boldsymbol{r}_2),\end{aligned} \tag{2}$$

where $\boldsymbol{U}_n(\boldsymbol{r})$ and $\boldsymbol{R}_m(\boldsymbol{r})$ are the natural modes of the incident field and the detector's reception pattern, with indices n and m, respectively. Here, β_n stands for the occupancy of the mode n of the incident field, and α_m corresponds to the detector's absorption sensitivity to its mode with index m.

We can use Equation (2), expanding $\overline{\overline{\mathbf{E}}}(\boldsymbol{r}_1, \boldsymbol{r}_2)$ as an incoherent superposition of a set of fully spatially coherent fields,[7] to formulate an alternative picture of the problem, as one of coupled modes. The absorbed power then depends on how the field modes project into the detector modes. The former are formally defined by the eigenvalue equation

$$\int_{\mathcal{S}} \overline{\overline{\mathbf{E}}}(\boldsymbol{r}_1, \boldsymbol{r}_2) \cdot \boldsymbol{U}_m(\boldsymbol{r}_2) d^2\boldsymbol{r}_2 = \beta_m \boldsymbol{U}_m(\boldsymbol{r}_1), \tag{3}$$

subject to the nomarlization

$$\int_{\mathcal{S}} \boldsymbol{U}_m^*(\boldsymbol{r}) \cdot \boldsymbol{U}_n(\boldsymbol{r}) d^2\boldsymbol{r} = \delta_{mn} \qquad \forall m, n. \tag{4}$$

Substituting the decomposed forms from Equation (2) into Equation (1) and using the Hermicity of $\overline{\overline{\mathbf{D}}}(\boldsymbol{r}_1, \boldsymbol{r}_2)$, we obtain

$$\langle P \rangle = \sum_{m,n} \alpha_m \beta_n |S_{mn}|^2, \tag{5}$$

where

$$S_{mn} = \int_{\mathcal{S}} \boldsymbol{R}_m^*(\boldsymbol{r}) \cdot \boldsymbol{U}_n(\boldsymbol{r}) d^2\boldsymbol{r} \tag{6}$$

is the overlap between natural mode m of the detector and natural mode n of the field.

2.2 Experimental characterization

Now that we have parametrized the optical behavior of a detector using the DRF, we turn to its characterization. Consider N possible three-dimensional positions to which an electromagnetic probe can be moved, producing the corresponding non-orthogonal vector field set $\mathbb{E} = \{\boldsymbol{e}_n(\boldsymbol{r}), \forall n \in \{1, ..., N\}\}$. By definition, the elements of $\overline{\overline{\mathbf{D}}}(\boldsymbol{r}_1, \boldsymbol{r}_2)$ in the basis $\mathbb{E}$ are

$$D_{nn'} = \iint_{\mathcal{S}^2} \boldsymbol{e}_n^*(\boldsymbol{r}_1) \cdot \overline{\overline{\mathbf{D}}}(\boldsymbol{r}_1, \boldsymbol{r}_2) \cdot \boldsymbol{e}_{n'}(\boldsymbol{r}_2) d^2\boldsymbol{r}_1 d^2\boldsymbol{r}_2. \tag{7}$$

Because the set $\{\boldsymbol{e}_n\}$ is not necessarily orthogonal, we reconstruct $\overline{\overline{\mathbf{D}}}(\boldsymbol{r}_1, \boldsymbol{r}_2)$ via

$$\overline{\overline{\mathbf{D}}}(\boldsymbol{r}_1, \boldsymbol{r}_2) \approx \sum_{n,n'} D_{nn'} \tilde{\boldsymbol{e}}_n(\boldsymbol{r}_1) \tilde{\boldsymbol{e}}_{n'}^*(\boldsymbol{r}_2), \tag{8}$$

where $\tilde{\mathbb{E}} = \{\tilde{\boldsymbol{e}}_n(\boldsymbol{r}), \forall n \in \{1, ..., N\}\}$ is the dual set of $\mathbb{E}$: this equation describes the reconstruction of the DRF in the spatial basis, on the chosen integration surface $\mathcal{S}$, from matrix elements $D_{nn'}$ of the DRF in the basis of source positions. Equation (8) is an equality only if the basis $\mathbb{E}$, and hence its dual $\tilde{\mathbb{E}}$, is complete or overcomplete. Note that we make no assumptions about the forms of the source fields $\boldsymbol{e}_n(\boldsymbol{r})$ and their duals; for instance, there is no restriction on the distance between the probe and the detector surface, such that the results above are valid in the near-field, far-field and intermediate cases.

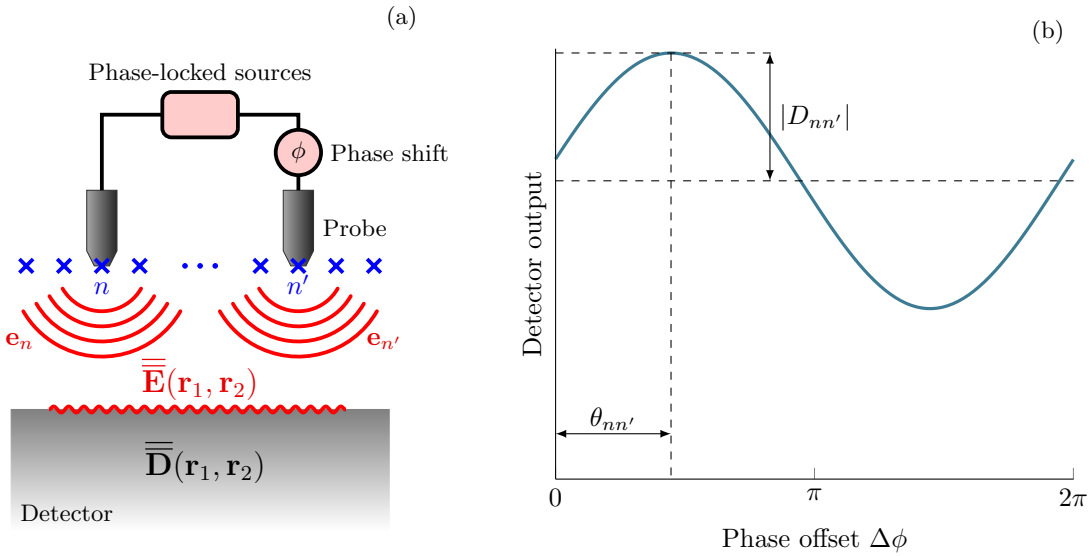

Figure 1: Experimental arrangement for measuring the $D_{nn'}$ element of the DRF. The detector under test is illuminated with a two phase-locked probes. When the phase of one source is rotated relative to the phase of the other, the detector output produces a fringe pattern. Its complex amplitude gives information about the DRF in the basis of source locations. (a) Experimental arrangement. (b) Fringe pattern.

To recover the matrix elements $D_{nn'}$, Equation (7) implies that we need probes at locations labeled n and n' simultaneously. We therefore consider the case where the incident field $\boldsymbol{E}(\boldsymbol{r})$ is generated by two phase-locked coherent sources, with relative phase difference ϕ. Denoting sources 1 and 2 at positions n and n' respectively, we can write the field $\boldsymbol{E}(\boldsymbol{r})$ as

$$\boldsymbol{E}(\boldsymbol{r}) = \boldsymbol{e}_n(\boldsymbol{r}) + \boldsymbol{e}_{n'}(\boldsymbol{r})e^{i\phi}. \tag{9}$$

This experimental configuration is summarized in Fig. 1. Using the definition of $\overline{\overline{\mathbf{E}}}(\boldsymbol{r}_1, \boldsymbol{r}_2)$ with Equation (9), and substituting into Equation (1):

$$\langle P \rangle = D_{nn} + D_{n'n'} + 2|D_{nn'}| \cos(\phi + \theta_{nn'}), \tag{10}$$

where we have used the definition of dual vectors $\int_{\mathcal{S}} \tilde{\boldsymbol{e}}^*_m(\boldsymbol{r})\boldsymbol{e}_n(\boldsymbol{r})d^2\boldsymbol{r} = \int_{\mathcal{S}} \tilde{\boldsymbol{e}}_m(\boldsymbol{r})\boldsymbol{e}^*_n(\boldsymbol{r})d^2\boldsymbol{r} = \delta_{mn}$, and the Hermicity of $\overline{\overline{\mathbf{D}}}(\boldsymbol{r}_1, \boldsymbol{r}_2)$ such that $D^*_{nn'} = D_{n'n}$. $|D_{nn'}|$ and $\theta_{nn'}$ are the magnitude and phase of $D_{nn'}$ respectively. The last term is proportional to $\cos(\phi)$: by varying the phase difference ϕ, we obtain fringes as in Fig. 1. These allow us to extract all of the parameters in the expression, and hence information concerning the detector response function $\overline{\overline{\mathbf{D}}}(\boldsymbol{r}_1, \boldsymbol{r}_2)$.

In practice, we can use Equation (10) to populate the response matrix $D_{nn'} \in \mathbb{C}^{N\times N}$. Single-source measurements can be used to determine its diagonal elements, using $P^0_{nn} = D_{nn}$: the fringe amplitude is simply the single-source DC measurement. Off-diagonal elements of D, where the sources are located in positions $n \neq n'$ can be then populated using measurements for various phase offsets ϕ; the simplest form is obtained when $\phi \in \{0, \pi/2\}$, corresponding to a $\cos(\theta_{nn'})$ and $\sin(\theta_{nn'})$ term in Equation (10), respectively. We can then split measurement data into three types:

$$\begin{cases} P^0_{nn} = D_{nn} \\ P^c_{nn'} = D_{nn} + D_{n'n'} + 2\Re\{D_{nn'}\} \\ P^s_{nn'} = D_{nn} + D_{n'n'} - 2\Im\{D_{nn'}\}, \end{cases} \tag{11}$$

where the first line corresponds to single-source measurements. This can be rearranged to obtain the elements

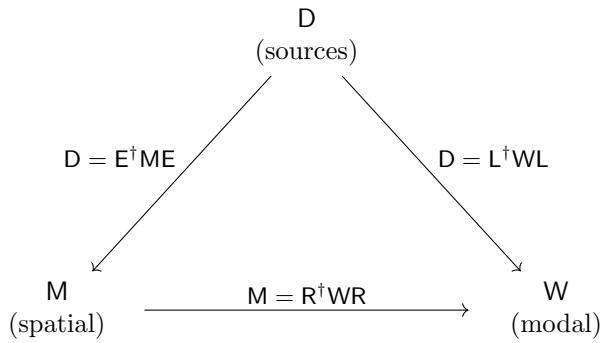

Figure 2: Diagram of the relations between the different matrix representations; the basis of each matrix is stated in parentheses.

of $D_{nn'}$ in terms of the measurements:

$$\begin{cases} D_{nn} = P^0_{nn} \\ \Re\{D_{nn'}\} = (P^c_{nn'} - P^0_{nn} - P^0_{n'n'})/2 \\ \Im\{D_{nn'}\} = -(P^s_{nn'} - P^0_{nn} - P^0_{n'n'})/2. \end{cases} \tag{12}$$

2.3 Matrix formulation for data analysis

In order to obtain a formulation suitable for data analysis and computational studies, we turn to matrix notation instead of dyadics. This is particularly useful to deal with experimental situations including finite sampling and non-point like sources. We start with the discretization of the detector surface $\mathcal{S}$ into J sample points, and the discretization of the dyadic $\overline{\overline{\mathbf{D}}}(\boldsymbol{r}_1, \boldsymbol{r}_2)$ into a matrix M over these sample points. We can write Equation (8) in a form that more explicitly conveys the change of basis, from that of source fields to the spatial representation, as

$$\mathsf{M} = \tilde{\mathsf{E}}\mathsf{D}\tilde{\mathsf{E}}^\dagger. \tag{13}$$

Here, the components of the measurement matrix D are given to $D_{nn'}$, related to the power measurements as above. We compute $\tilde{\mathsf{E}}$ by taking the dual of the matrix E of field patterns: its n^{th} column corresponds to e_n, the discretized version of the single-source field $\boldsymbol{e}_n(\boldsymbol{r})$ over the J discrete sample poins of the integration surface $\mathcal{S}$. Again, we stress that $\mathcal{S}$ can be any surface of integration where the probe fields are known, and not restricted to either the source plane or detector plane. Similarly, we can write the general form for the response matrix in basis of source fields:

$$\mathsf{D} = \mathsf{E}^\dagger\mathsf{M}\mathsf{E}. \tag{14}$$

Note that this can be seen as a deconvolution of the detector's response to the field in the detector plane, $\mathsf{M} \in \mathbb{C}^{J\times J}$, into the detector's response to sources in the basis of source locations, $\mathsf{D} \in \mathbb{C}^{N\times N}$. In some experimental cases, we may actually not wish to use this transformation.

Both matrices, D and M, can then be diagonalized to obtain the eigenvectors and eigenvalues of the detector response function:

$$\begin{aligned} \mathsf{D} &= \mathsf{L}^\dagger\mathsf{W}\mathsf{L} \\ \mathsf{M} &= \mathsf{R}^\dagger\mathsf{W}\mathsf{R}, \end{aligned} \tag{15}$$

where W is the diagonal matrix of eigenvalues, corresponding to relative sensitivities of the DRF to modes given column-wise in L (for representation in the basis of source fields) and R (for representation in the spatial basis). Each column of $\mathsf{R}(\boldsymbol{r})$ corresponds to one of the modes $\boldsymbol{R}$ from Equation (2), discretized over the detector surface as chosen to construct the matrix E above. The elements of L are then given by $\mathsf{L}_{mn} = \int_{\mathcal{S}} \boldsymbol{R}_m(\boldsymbol{r}) \cdot \boldsymbol{e}_n(\boldsymbol{r}) d^2\boldsymbol{r}$. The matrix form $\mathsf{L} = \mathsf{R}^\mathsf{T}\mathsf{E}$ tends to the integral form above for an infinite number of sample points J over the integration surface. The various transformations between representation bases are summarized in Fig. 2.

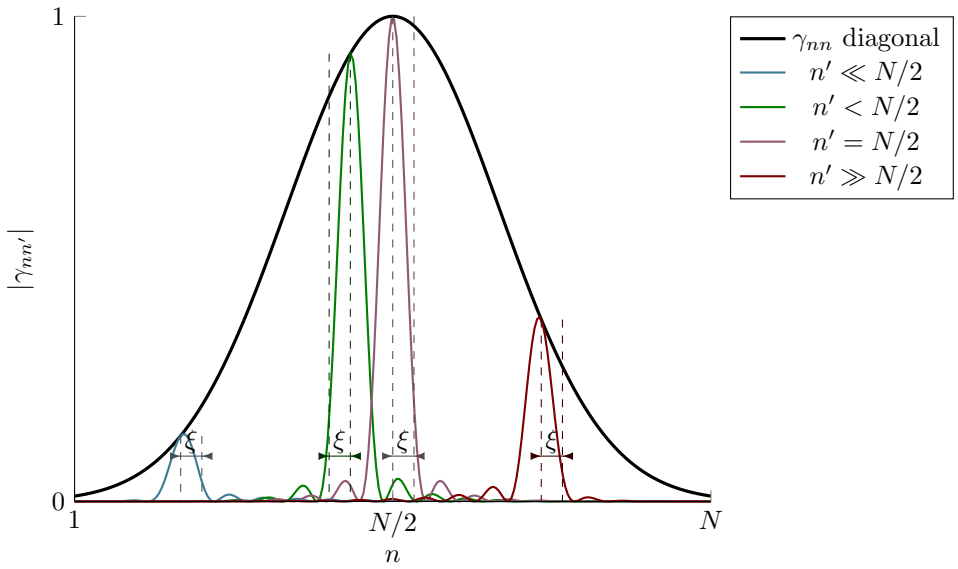

Figure 3: Illustrative plot of $|\gamma_{nn'}|$, showing how the coherence length ξ can be extracted; a single source scans through N uniformly distributed positions, while the second source is fixed at position n'.

Substituting Equation (14) into Equation (13), we obtain the measured response matrix M' in terms of the actual response matrix M:

$$\mathsf{M}' = \tilde{\mathsf{E}}\mathsf{E}^\dagger \mathsf{M} \mathsf{E}\tilde{\mathsf{E}}^\dagger. \tag{16}$$

If the measurement set $\mathbb{E}$ is complete or overcomplete, i.e. if dual vectors $\tilde{\mathsf{e}}_n$ are contained in the rows of $\tilde{\mathsf{E}}$, then by definition $\mathsf{E}\tilde{\mathsf{E}}^\dagger = \tilde{\mathsf{E}}\mathsf{E}^\dagger = \mathsf{I}_{J\times J}$. In that case, $\mathsf{M}' = \mathsf{M}$: we can completely retrieve the response matrix from the measured matrix. In the opposite case, where the measurement source fields do not completely span the fields to which the power is sensitive, we use Singular Value Decomposition (SVD) to compute the pseudo-inverse matrices:

$$\mathsf{E} = \mathsf{U}\Sigma\mathsf{V}^\dagger \implies \mathsf{E}\tilde{\mathsf{E}}^\dagger = \mathsf{U}\Sigma\Sigma^{-1}\mathsf{U}^\dagger, \tag{17}$$

where Σ is diagonal. Equation (17) corresponds to the projection of the natural modes onto measurement space, followed by the application of a diagonal filter, and the reconstruction of the measured modes; information is lost in the imperfect filtering step. An EAI experiment must therefore be designed carefully to capture all required information.

2.4 Experimental strategies

At first, it may seem as though a large number of measurements is needed, to iterate over all possible pairs of source positions. However, many methods can be used to circumvent this apparent requirement and exploit available redundancies. For instance, real-time analysis is possible, even with incomplete data and an undercomplete set of basis vectors. Using incremental SVD (iSVD) on successive matrices constructed from data taken,[?] it is possible to iteratively check whether sufficient data has been taken. The iSVD technique will converge when there is sufficient information to find all degrees of freedom, i.e. natural modes. This is particularly applicable to cases where the number of modes to be recovered is unknown, and can potentially minimize the number of measurements required.

Where the number of natural modes of the detector response is unknown, we may ask whether the minimum number of measurements necessary is finite at all.[9] The number of measurements required goes as $\propto \mathcal{O}(N^2)$, because we need to fill in $\mathsf{D} \in \mathbb{C}^{N\times N}$; on the other hand, the amount of information required to reconstruct the modes in the system goes at maximum as $\propto \mathcal{O}(mN)$, because the information required grows as the number of modes m and the number of eigenvalues of a $N \times N$ matrix. Therefore, any data analysis algorithm will eventually converge, when a complete set of measurement fields is attained: the measured detector response then matches the actual response, and the detector's modes can be recovered.

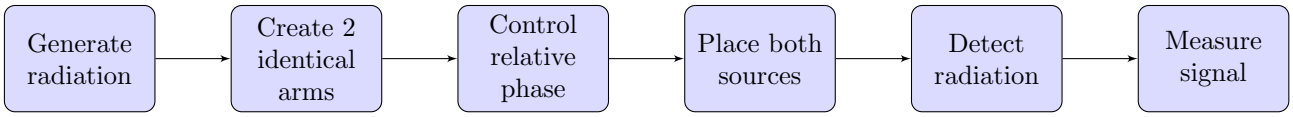

Figure 4: Flow chart of the proposed EAI experimental system.

When considering methods for scanning the two probes, it is important to note that EAI is insensitive to the choice of the source locations and their indexing order. This implies that scanning strategies can be devised in order to minimize the required number of measurements for measurement set $\mathbb{E}$ to be complete. We are currently investigating this through numerical methods, for instance to assess the difference between Cartesian grids, polar grids, and sets of random locations, over different scanning ranges and for various scanning densities.

Even sweeping a single source with the other fixed can yield significant results about the detector response. For instance, the matrix of complex visibilities $\gamma_{nn'}$ is related to the elements of D as follows:

$$\gamma_{nn'} = \frac{2D_{nn'}}{D_{nn} + D_{n'n'}}. \tag{18}$$

By moving along the row n of D, we plot $|\gamma_{nn'}|$: this reveals the transverse and longitudinal coherence lengths, areas and volumes, as shown in Fig. 3 for the case of a one-dimensional scan. We may then obtain the coherence length graphically, subject to choosing an appropriate cutoff value in $|\gamma_{nn'}|$, which goes to 0 as the distance between the sources is increased. We remark that phase information is not even necessary for this process: $|\gamma_{nn'}|$ and related quantities, such as a rough estimate of the number of modes, can be recovered using only the amplitude of elements in row n of the matrix $D_{nn'}$, and its diagonal $D_{nn} \in \mathbb{R}$.

3. EXPERIMENTAL REALIZATION

3.1 System requirements

We now turn to the design of an experimental system for EAI at near-infrared wavelengths. As described by the theory, we can obtain all of the information about a power detector's state of coherence by measuring the fringes in the detector's output as we modulate the phase difference between two phase-locked sources. In the description below, we discuss the design choice for an experiment at $\lambda = 1550$ nm wavelength: this particular choice is mostly guided by the large range of commercially-available components, because 1550 nm is a standard wavelength in the telecommunications industry. All of these considerations however hold for the broader near-infrared range. This first section describes the general requirements for such an experiment, which are analogous to those of the millimeter-wavelength EAI experiment performed by Thomas,[3] while the following section discusses specific choices for our experimental realization.

Starting from the EAI theory described above, various basic technical capabilities are required to complete the tasks summarized as a block diagram in Fig. 4. First of all, we need a $\lambda = 1550$ nm source: it is clear that any experimental method can be simplified by considering the case of identical highly-coherent phase-locked probes with well-defined polarization, such that they can be considered quasi-monochromatic. For instance, a narrow-linewidth laser corresponds ideally. Its radiation coherence length Δx must be far greater than the differential optical path length, with

$$\Delta x \approx \frac{c}{\Delta\nu} \approx \frac{\lambda^2}{\Delta\lambda}, \tag{19}$$

where λ is the central wavelength, and $\Delta\lambda$ and $\Delta\nu$ are the radiation linewidth in length and frequency units, respectively. At $\lambda = 1550$ nm, we have the following equivalence: $\Delta x = 1$ m $\leftrightarrow \Delta\lambda = 2.4$ pm $\leftrightarrow \Delta\nu = 300$ MHz. Because the maximum optical path length will be at most of the order of meters, a source with $\Delta\nu < 1$ MHz is by far sufficient.

In order to obtain two phase-locked, coherent probes, we may synchronize two laser sources or use a 50/50 beamsplitter with a single source, followed by delay lines to adjust the path lengths of each arm, and phase modulators to control the relative phase difference. Freespace and fiber-based systems are both possible, and we

Component	Typical insertion loss (dB)
Beamsplitter (input to single output)	3.6 ± 0.2
Delay line	1.5 ± 0.3
Phase modulator	3.2 ± 0.5
Fiber connections (with index-matching gel)	0.5 ± 0.1
Propagation in optical fiber ($\mathcal{O}$(1m) length)	< 0.01

Table 1: Table of expected losses from each component in the proposed fiber-based system.

choose to discuss the case of a fiber-based experiment here. In order to determine the required power output of the laser, it is necessary to know the ratio between the power output of the laser and of the sources, even though there is some flexibility on the absolute power. Optical power loss comes mainly from insertion loss in the different components of the circuit. While losses are low for freespace systems, typical experimental values for fiber-based systems are given in Tab. 1. Summing these contributions, and assuming 3 connectors are on the path of each source (beamsplitter to delay line, delay line to phase modulator, phase modulator to source fiber), the expected total loss is $\approx$ 10 dB, i.e. a reduction by a factor 10: a laser with optical power output 50 mW implies two fiber sources of 5 mW each.

Some scanning system is necessary to move the two sources precisely to relevant position pairs, and should preferably motorized and programmable. In order to find constraints on scanning ranges and accuracy, we must first compute the minimum sampling of the detector beam pattern. Using the Nyquist-Shannon sampling theorem, we can obtain a rough upper bound on the step size Δx between measurement locations, such that

$$\Delta x \leq \frac{1}{2C}. \tag{20}$$

The value C is determined by the larger of three lengths: (i) the source radiation's wavelength λ, (ii) the source diameter d_{source}, or (iii) the spot size of detector beam pattern $s(D)$ at orthogonal distance D from the source plane. Using $\lambda = 1550$ nm, the wavelength is always much smaller than the other two quantities in any reasonable experimental system. Moreover, because we will only consider diverging beams, $d_{source} < s(D)$ for any experimentally relevant D, so

$$\Delta x \leq \frac{s(D)}{4\pi}. \tag{21}$$

Assume that $s(D)$ is due to the detector core diameter d_{det} and the divergence angle θ of the virtual beam coming out of the detector, also called its acceptance angle, related its numerical aperture $\mathrm{NA}_{det} = \sin(\theta)$. Then, the accuracy of the scanning system must be better than

$$\Delta x^{max} = \frac{2z \tan(\sin^{-1}(\mathrm{NA}_{det})) + d_{det}}{4\pi}. \tag{22}$$

This is of the order of millimeters for slightly divergent beams and distances between the source and detector planes of a few centimeters.

The detector under test is read out with an amplifier, to provide a suitably large signal. We should also note that the fringe amplitude is proportional to the field amplitude of each source, whereas the DC term is equal to the sum of squares of the sources' respective fields. The signal-to-noise ratio (SNR) of the measurement system should be sufficiently high to measure fringes even when either or both sources are far off-axis from the detector and coupling minimal power. The definition of this minimal power should be chosen to be for the outermost location in the sampling grid selected; it will be at most the radius of the circle drawn by the detector's numerical aperture when projected on the source plane. Finally, we need a way of acquiring and digitizing this signal data, in order to obtain it in a form suitable for the reconstruction of the DRF matrix and the analysis process described in the previous section.

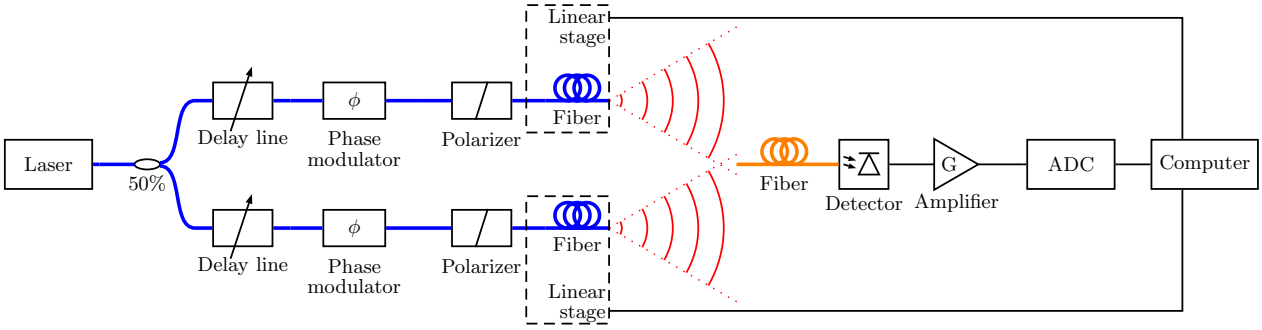

Figure 5: Block diagram of the proposed EAI experimental system; blue fibers are single-mode and polarization maintaining; the orange fiber is interchangeable.

Name	Symbol	Units	Values		
Aperture-detector orthogonal distance	D	mm	50	100	100
Detector diameter	d_{det}	μm	9.5	9.5	50
Detector numerical aperture	NA_d		0.13	0.13	0.22
Source e^{-2} power radius at D		mm	0.5	1.0	1.0
Max power on detector at D	$P(r=0)$	nW	9.3	2.3	64
Maximum step size at D	Δx^{max}	mm	1.0	2.1	3.6
Mode number estimate	N_{modes}		Single	Single	Multi

Table 2: Table of computed values (bottom) for given fixed values (top), with power at output of fiber $P_{tot} = 5$ mW and fiber spot size $w_0 = 5$ μm, at wavelength $\lambda = 1550$ nm.

3.2 System detail

Now that we have discussed the general requirements of an EAI experiment at near-infrared wavelength, we present the specific choices we have made for our experimental realization. We have chosen to build a fiber-based system, because using optical fibers simplified the source scanning apparatus for two-dimensional and three-dimensional grids compared to the freespace systems we considered.

As part of our experimental realization, we have chosen a 10 kHz linewidth, 18 dBm output power laser source, a 50/50 fiber-based beamsplitter to create two identical arms, fiber-based phase modulators to control their relative phase, with embedded linear polarizers to ensure high-quality polarization, and polarization-maintaining fibers with FC/APC connectors so that the polarization remains well-defined throughout the optical fiber system. The source fibers emit the laser radiation into freespace, and are mounted on two sets of three-axis, computer-controllable, linear stage systems with a positioning accuracy of 4 μm and 10 cm range.

Our demonstration detector is a 1.2 GHz-bandwidth, low-noise InGaAs photodiode detector with sub-nanoamp dark current and a maximum NEP of order 1 fW/$\sqrt{\mathrm{Hz}}$. As this detector acts as a current source and has approximately 1 A/W responsivity, a high-gain, low-noise transimpedance amplifier is required to convert currents as small as nanoamps into a measurable voltage signal. This signal can then be read out using an analogue-to-digital converters (ADC) connected to a computer; we chose a 16-bit ADC with 250 kHz bandwidth to allow for precise and rapid measurement, even for fringe frequencies of the order of several kilohertz.

For typical values of properties from commercially-available components, we compile the requirements in Table 2. Our experimental system, summarized as a block diagram in Fig. 5 and shown in photograph in Fig. 6, fulfills the requirements discussed in this section.

3.3 Mode filtering

While the semiconductor photodetector purchased is expected to be highly-multimode, we wish to build a detector system capable of synthesizing various modal responses. We do so by coupling the detector to different moded optical fibers to act as modal filters, such that we obtain a wide range of mode reconstruction problems. Using

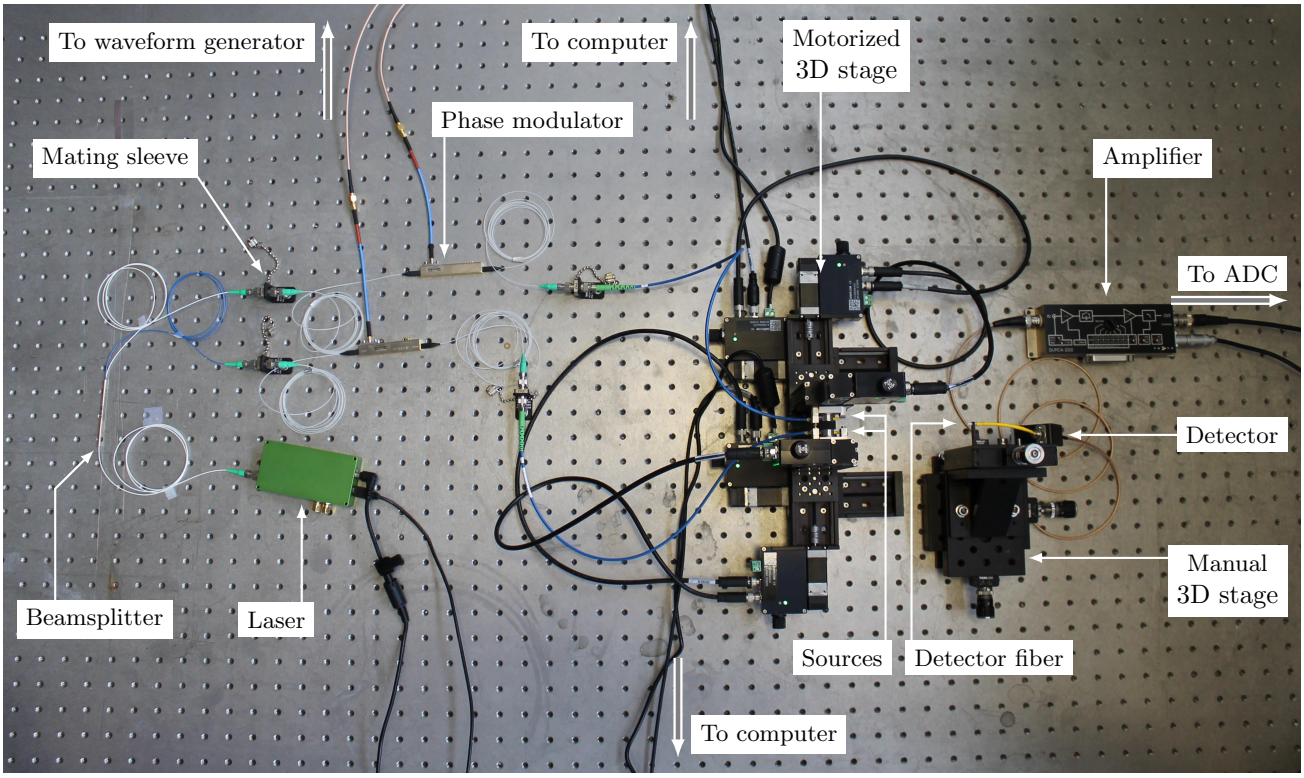

Figure 6: Labeled picture of the experimental system, to be enclosed after initial tests are completed.

an optical fiber introduces two advantages: (i) fibers can be selected and changed to obtain the modal constraints desired, and (ii) we can estimate the number of modes of a step-index multi-mode fiber, and obtain a reliable lower bound to the number of modes in the case of a few-mode fiber.

First, a fiber's V-value V is defined[10] as

$$V = \frac{2\pi}{\lambda} a \times \mathrm{NA}, \tag{23}$$

where λ is the operating wavelength, a is the fiber radius and NA its numerical aperture. If a fiber has $V < 2.405$, it is single-mode at that wavelength. For highly multi-mode fibers, the number of modes N can be approximated by

$$N = \frac{A\Omega}{\lambda^2} \approx \frac{V^2}{4}. \tag{24}$$

where A is the fiber core area and Ω is the fiber beam pattern's solid angle, taken as a cone with half-angle $\theta = \sin^{-1}(\mathrm{NA})$. In particular, it should be noted that fibers labeled as single-mode, but with a second-mode cutoff wavelength slightly higher than the operation wavelength, can be used as few-moded fibers. For instance, a fiber with second-mode cutoff wavelength $\lambda_0 = 1700$ nm is two-moded at $\lambda = 1550$ nm.[11] Equation can be used as a lower bound to confirm this result. Using that $V = 2.405$ at $\lambda_0 = 1700$ nm, we obtain that $V(\lambda = 1550\ \mathrm{nm}) = 2.405 \times 1.7/1.55 \approx 2.64$, and $N \approx 1.74 \sim 2$.

The detector we have chosen has an FC/PC connector input, such that any piece of optical fiber with a male connector can be used: we can therefore very simple change the detector, in order to apply a different modal filter, and thus effectively construct a large variety of detector-plus-fiber systems. While the optical fibers used are all different, the steps to adapt them to our experiment are identical: we cleave a piece of optical fiber, connectorize one end with an FC/PC connector and the other with a ceramic ferrule, protect the system with 900 μm plastic tubing and heatshrink, and polish both connector faces. The current set of detector fibers considered is summarized in Table 3.

Fiber name	Core diameter	Numerical aperture	Type
Thorlabs 1550BHP	$9.5\mu m$	0.13	Single-mode
Thorlabs SM2000	$11\mu m$	0.11	Few-mode
Thorlabs FG050LGA	$50\mu m$	0.22	Multi-mode
Thorlabs FG105LCA	$105\mu m$	0.22	Multi-mode
Thorlabs FG105LVA	$105\mu m$	0.10	Multi-mode

Table 3: Table of some commercially-available fibers and their expected mode type.

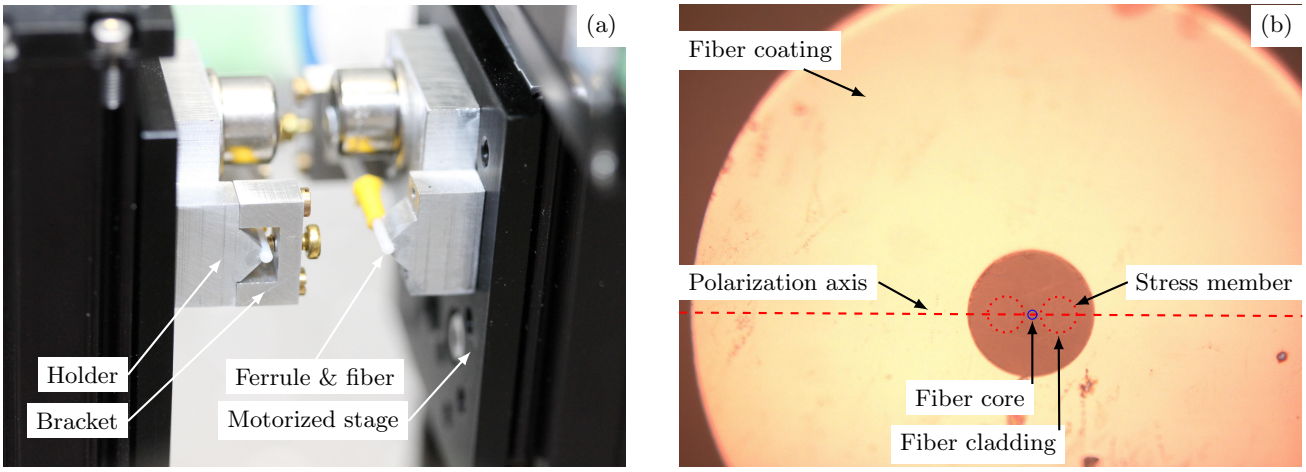

Figure 7: Custom equipment for the source fibers, built from a polarization-maintaining fiber with an FC/APC connector and a ceramic ferrule, placed in a custom holder; the bracket is removed once the ferrule is glued. (a) Open end of the source fiber, inside a ceramic ferrule; left ferrule is secured in the holder by a bracket. (b) Microscope picture of the polished face of a polarization-maintaining fiber, with 200× magnification.

3.4 Sources

With our goal being to measure fringes for each source location pair over some predefined sampling grid, we need to pay particular attention to the capability to bring the sources as close together as possible. Ideally, the positioning system should be able to place them accurately in two neighboring locations. While having both sources at the same location is impossible in practice, we should note that this is also unnecessary, as the fringe amplitude is simply the single-source DC measurement. We have therefore also manufactured custom fiber holders to optimize the minimal physical distance between the sources, defined by the source fibers' cores. For each arm of the experiment, we used a piece of polarization-maintaining optical fiber with an FC/APC connector on one end and a ceramic ferrule on the other: the ferrule was inserted into a V-shaped groove, clamped down and glued, as shown in Fig. 7; the plastic tubing around the fiber, about 3cm behind the ferrule, was also glued to provide stress relief. By removing the clamps, we are then able to reduce the distance between the sources' fiber cores to two ferrule radii, corresponding here to 1.25mm.

An important procedure is to make sure that the polarizations of the two sources are aligned, before the gluing step. We have found that we obtain satisfactory results by looking at the polished face of the fiber's open end under a microscope: the stress members of the so-called "panda-style" polarization-maintaining fiber we chose are sufficiently visible to be used as an axis, as shown in Fig. 7. This can then be aligned with a feature of the custom holder, for instance the v-shaped groove, to establish a well-defined polarization axis. Here, we choose to align the polarization axes of the two probes. However, the same method could be used to create probes with non-aligned polarization axes, in order to measure the polarization-dependent behavior of the detector response for instance.

4. CONCLUSION

In this paper, we have described an experimental realization of Energy-Absorption Interferometry at near-infrared wavelengths. EAI is performed by illuminating a detector's surface using two monochromatic, coherent, phase-locked sources. By rotating their relative phase, the detector output displays a fringe. Repeating this process over source location pairs, and over polarizations where appropriate, we can reconstruct the detector response function, which fully characterizes the detector's optical behavior. By writing the DRF as an incoherent sum of modes, their full spatial forms and relative responsivities can be recovered, even when the number of modes is unknown. Then, we summarized the design process for an EAI experiment at 1550 nm wavelength, to be used to characterize commercially-available near-infrared detectors and map the modes of simple optical fibers. EAI provides a method for measuring the DRF and its decomposition in terms of the detector's natural modes; both are particularly important to the design of optical instruments, among many others.

EAI has a large number of other potential applications, far beyond what we have described here. For instance, it should be noted that EAI applies to the entire electromagnetic spectrum. Furthermore, it was shown by Saklatvala that the photon noise behavior of a detector is also characterized by the DRF, such that EAI can also reconstruct this contribution.[5] EAI can also be used for the study of correlations between detectors in a single array.[4] It was also shown by Withington that EAI can be further generalized to account for quantum correlations and probes acting through different forces on the surface under test.[12] Each of these cases could give rise to an experimental demonstration of its own, improve our understanding of the coupling of incident fields into absorbing structures, reveal the influence of design choices such as geometries and fabrication properties, and allow the optimization of both detectors and any preceding instrumentation. The experimental demonstration for the case of near-infrared detectors described here therefore also represents a strong step forward towards each of these goals.

ACKNOWLEDGMENTS

Dan Moinard is funded by a studentship from the Science and Technology Facilities Council, United Kingdom, and acknowledges financial support from the Cambridge CDT in Nanoscience and Nanotechnology.

REFERENCES

[1] Withington, S. and Saklatvala, G., "Characterizing the behaviour of partially coherent detectors through spatio-temporal modes," *Journal of Optics A: Pure and Applied Optics* **9**, 626–633 (jul 2007).

[2] Withington, S. and Thomas, C. N., "Probing the dynamical behavior of surface dipoles through energy-absorption interferometry," *Physical Review A* **86**, 043835 (oct 2012).

[3] Thomas, C. N. and Withington, S., "Experimental Demonstration of an Interferometric Technique for Characterizing the Full Optical Behavior of Multi-Mode Power Detectors," *IEEE Transactions on Terahertz Science and Technology* **2**, 50–60 (jan 2012).

[4] Saklatvala, G., Withington, S., and Hobson, M. P., "A coupled-mode theory for infrared and submillimeter wave detectors," in [*6275, Millimeter and Submillimeter Detectors and Instrumentation for Astronomy III*], *Proc. SPIE* **6275**, 62750W–62750W–12 (2006).

[5] Saklatvala, G., Withington, S., and Hobson, M. P., "Coupled-mode theory for infrared and submillimeter wave detectors," *Journal of the Optical Society of America A* **24**(3), 764 (2007).

[6] Withington, S., Thomas, C., and Goldie, D., "Partially Coherent Optical Modelling of the Ultra-Low-Noise Far-Infrared Imaging Arrays on the SPICA Mission," *arXiv preprint arXiv:1307.7278* (jul 2013).

[7] Mandel, L. and Wolf, E., [*Optical coherence and quantum optics*], Cambridge University Press, Cambridge (1995).

[8] Sarwar, B., Karypis, G., Konstan, J., and Riedl, J., "Incremental Singular Value Decomposition Algorithms for Highly Scalable Recommender Systems," *Proceedings of the Fifth International Conference on Computer and Information Technology (ICCIT)* , 1–6 (2002).

[9] Thomas, C. N., *Theoretical , Numerical and Experimental Studies of the Optical Behaviour of Few-Mode Power Detectors for Submillimetre and Far-Infrared Astronomy*, PhD thesis, University of Cambridge (2012).

[10] Snyder, A. W. and Love, J. D., [*Optical Waveguide Theory*], Springer US, Boston, MA (1984).

[11] Li, A., Wang, Y., Hu, Q., and Shieh, W., "Few-mode fiber based optical sensors," *Optics Express* **23**, 1139 (jan 2015).

[12] Withington, S., Thomas, C. N., and Goldie, D. J., "Probing Quantum Correlation Functions Through Energy Absorption Interferometry," *arXiv preprint arXiv:1609.03174* (sep 2016).